Journal of Materials Chemistry A

PAPER

View Article Online
View Journal | View Issue

Cite this: J. Mater. Chem. A, 2018, 6, 9057

ZnO nanosheets with atomically thin ZnS overlayers for photocatalytic water splitting†

Xu Zhang,[a] Yu-Zhu Zhou,[a] De-Yao Wu,[a] Xiao-Hua Liu,[a] Rui Zhang,[a] Hui Liu,[a] Cun-Ku Dong,[a] Jing Yang,*[a] Sergei A. Kulinich*[b] and Xi-Wen Du*[a]

Zinc oxide is a cost-efficient and eco-friendly material for solar-to-chemical energy conversion. However, the relatively wide band gap and poor stability restrict its practical applications. Herein, we report on the modification of ZnO nanosheets with a porous atomically thin ZnS overlayer. The as-prepared ZnS/ZnO/ZnS sandwich nanosheets exhibit a reduced band gap (2.72 eV) and yet a slightly elevated conduction band minimum, which remarkably broadens the wavelength range for light absorption and generates electrons with enough reducing capability. At the same time, the newly-prepared sandwich nanosheets possess alternatively exposed ZnS and ZnO surface patches, which attract and accommodate photogenerated holes and electrons, respectively. In addition, the ZnS overlayer catalyzes and accelerates hole-consumption reactions, thus preserving electrons for efficient water splitting. As a result, the ZnS/ZnO/ZnS sandwich nanosheets demonstrate intensive light absorption, fast charge separation, long electron lifetime, and eventually the highest hydrogen production rate reported for oxide catalysts so far. This work proves that passivation with an ultrathin layer is a potent approach for energy-band engineering, and semiconductor sandwich nanostructures are promising for highly efficient water splitting under sunlight.

Received 26th February 2018
Accepted 11th April 2018

DOI: 10.1039/c8ta01846d

rsc.li/materials-a

Introduction

Water photolysis under sunlight irradiation is an intriguing strategy toward recyclable and clean hydrogen energy.[1,2] The hydrogen evolution reaction (HER) is usually driven by semiconductor photocatalysts and consists of three sequential steps, *i.e.*, generation of electron–hole pairs caused by light irradiation, charge separation and migration to the catalyst surface, and H_2 production *via* H_2O reduction.[3–5] Hence an ideal photocatalyst for the HER is expected to possess at least the following three characteristics. First, its moderate band gap should be wide enough (>2.0 eV) to overcome the energy barrier for water splitting[6] and narrow enough (<3.0 eV) to absorb sunlight efficiently.[6] Second, the material should transfer its photogenerated carriers at the lowest possible recombination rates. And finally, its conduction-band minimum should be more negative than the proton reduction potential (H^+/H_2).[7–10] Notwithstanding the relative simplicity of these requirements, most of the photocatalytic materials developed thus far cannot meet all three simultaneously.

The most popular catalysts for water photolysis can be divided into three categories: (i) chalcogenides (*e.g.* CdS and ZnS),[10–12] (ii) nitrides (or oxynitrides, such as TaON,[13] Ta_3N_5 (ref. 14) and g-C_3N_4 (ref. 15)), and (iii) oxides (*e.g.* TiO_2 and ZnO).[16–18] Among the three classes, oxides have attracted much interest because of environmental and economic advantages. However, their large band gaps hinder efficient light absorption in the wide spectrum range.[19] In addition, oxides usually suffer from severe recombination of photogenerated electron–hole pairs.[20]

Many efforts have been made to enhance light harvesting with oxides. One efficient way developed so far is based on the formation of a solid solution of two semiconductors, such as GaN–ZnO[21,22] and ZnO–ZnS,[23] which reduces their band gap. However, this strategy is usually known to downshift the conduction band, which is unfavourable for achieving excited electrons with high potential.[24] Another strategy is to generate defective levels in the band gap by introducing oxygen vacancies.[25] This approach, however, also has a drawback as the defects may cause serious recombination of electrons and holes.

In order to suppress charge recombination, noble metal or semiconductor co-catalysts were engineered to work together with oxide photocatalysts.[26–35] Noble metal co-catalysts were found to be very successful in accelerating charge separation.[26–28] However, their relatively high costs limit their

[a]Institute of New Energy Materials, School of Materials Science and Engineering, Tianjin University, Tianjin 300072, P. R. China. E-mail: xwdu@tju.edu.cn; yang_jing@tju.edu.cn

[b]Research Institute of Science and Technology, Tokai University, 4-1-1 Kitakaname, Hiratsuka-shi, Japan. E-mail: skulinich@tokai-u.jp

† Electronic supplementary information (ESI) available: Detailed synthetic procedures, characterization methods, calculations and additional experimental results. See DOI: 10.1039/c8ta01846d

application. On the other hand, semiconductor co-catalysts usually form type II heterostructures with oxides, such as CdS/ZnO,[29] CdS/ZnS,[52] CdS/$Zn_xCd_{1-x}S$,[53] CuO/ZnO,[30] ZnSe/ZnO[31] and ZnS/ZnO,[32–34] which favor the flow of carriers and charge separation. Nevertheless, the formation of such heterostructures also lowers the conduction band position and suppresses the reducing capability of photo-excited electrons.[35]

Two dimensional (2D) nanostructures possess many features that make them attractive for water-splitting related applications. Among such are their high specific surface area, short diffusion length for carriers to reach the surface, and often unique exposed surfaces.[36,37] More intriguingly, recent computational studies suggested that alternate ZnO and ZnS layers would form a novel composite with a remarkably reduced band gap: for instance, a band gap as small as 1.5 eV was predicted for alternately stacked 9 layers of ZnO and 1 layer of ZnS.[38] Therefore, 2D composites of ZnO/ZnS look very promising for both light absorption and water splitting. However, to date, preparing semiconductor hetero-layers with controllable thickness has been a technically difficult and challenging task, especially taking into account the precise regulation of components in the atomic layer.

In this study, for the first time, we demonstrate a facile synthetic route to prepare ZnS/ZnO/ZnS sandwich nanosheets (SNSs) with atomically thin surface ZnS layers. We first produced ultra-thin Zn nanosheets coated with thin porous ZnS layers on both sides and then converted the ZnS/Zn/ZnS template into ZnS/ZnO/ZnS SNSs *via* oxidation. The novel nanostructure exhibits a narrow band-gap of 2.72 eV, which is much smaller than those of both ZnO and ZnS components. Importantly, the outermost ZnS layer is capable of suppressing carrier recombination and accelerating hole consumption on its surface, thereby supplying long-lifetime electrons for hydrogen production. As a result, the newly prepared ZnS/ZnO/ZnS SNSs achieve a hydrogen evolution rate as high as 2080 mmol h^{-1} g^{-1}, which corresponds to a quantum efficiency of 34.7%, *i.e.* one of the highest values reported for oxide catalysts so far.

Experimental section

Synthesis of materials

All chemical reagents were of analytical grade and purchased from Aladdin. The ZnS/Zn/ZnS nanosheets were prepared *via* thermal evaporation in a two-zone quartz tube furnace. Cleaned FTO-coated glass, 1.0 g of metallic zinc powder (99.9%) and CS_2 were used as the substrate, zinc source and sulfur source, respectively. Before synthesis, the tube was exhausted to vacuum first and then filled with N_2 and CS_2 gas with flow rates of 8 and 2 sccm, respectively. Subsequently, the zinc powder and FTO substrate were heated to 693 and 493 K, respectively, and kept for 1 hour; meanwhile, the pressure in the tube was maintained at 2 Torr. Afterwards, the furnace was cooled down naturally to room temperature. As a result, the ZnS/Zn/ZnS nanosheets were grown as arrays on the FTO substrate. The ZnS/Zn/ZnS template was then heated in a muffle furnace at a temperature of 553 K for 1 h, by which they were oxidized to ZnS/ZnO/ZnS SNSs. For the synthesis of ZnO nanosheets, the above described ZnS/Zn/ZnS nanosheets on FTO were dipped into 20 ml of 30.0% hydrogen peroxide for 5 h, during which ZnS gradually changed into $ZnSO_4$ and Zn was oxidized to ZnO. The obtained product was washed with deionized water and ethanol, and then dried with air flow. For the synthesis of ZnS nanosheets, the ZnS/Zn/ZnS nanosheets on FTO were put into a tube furnace together with 1.0 g S powder (99.9%). The tube was first flushed with N_2 stream to remove air and then heated to 773 K and held at this temperature for 1 h under a pressure of 1.0 Torr; eventually, the SNSs were completely transformed into ZnS nanosheets.

Characterization of materials

The phase structures were investigated by using X-ray diffraction (XRD, Rigaku D/max 2500v/pc). Atomic force microscopy (AFM) measurements were done with a Veeco IIIa nanoscope in the tapping mode, and the sample was prepared onto a silicon substrate by drop drying the aqueous solution of the sample. Morphological observations were performed by means of a scanning electron microscope (SEM, Hitachi S-4500) and transmission electron microscope (TEM, FEI Tecnai G2 F20) equipped with a field-emission gun operated at 200 kV. The specific surface areas of catalysts were determined by the Brunauer–Emmett–Teller (BET) method with N_2 adsorption–desorption isotherms. X-ray photoelectron spectroscopy (XPS) analyses were performed using a Perkin Elmer 5100 system with a non-monochromatic Al anode X-ray source. The absorption spectra were recorded using a Hitachi 3010 UV-vis absorption spectrometer.

Evaluation of photocatalytic performance

The photocatalytic reactions were conducted in a three-neck round flask with a volume of 150 mL. Different amounts (5, 10, 15, 20, and 30 mg) of the as-prepared samples were first separated from the FTO substrate and dispersed into an aqueous solution of 0.35 M Na_2S (99.9%)/0.25 M Na_2SO_3 (99%) (40 mL) by sonicating for 5 min, and then the suspension was transferred into a three-neck flask. The flask was sealed and purged with argon gas for 10 min, while the suspension was stirred vigorously. During the photocatalytic measurements, the reaction flask was irradiated with a xenon arc lamp (with a power of 100 W) at room temperature and atmospheric pressure under constant stirring. Gaseous products were analyzed using a gas chromatograph (Shimadzu GC-2014) to determine the amount of H_2 produced every hour after reaction. The apparent quantum efficiency (AQE) and quantum efficiency (QE) were calculated using the following formulas (1) and (2):

$$\begin{aligned} \mathrm{QE} &= \frac{\text{number of reacted electrons}}{\text{number of incident photons}} \times 100\% \\ &= \frac{\text{number of evolved } H_2 \text{ molecules} \times 2}{\text{number of incident photons}} \times 100\% \end{aligned} \quad (1)$$

$$\mathrm{AQE} = \frac{\text{number of photons used to generate } H_2}{\text{number of incident photons}} \times 100\% \quad (2)$$

A standard three-electrode system was applied for electrochemical measurements, with the as-prepared materials as working electrodes, HgO/Hg in 1 M KOH solution as the reference electrode and Pt foil as the counter electrode. The results were recorded using a VersaSTAT 3 Potentiostat electrochemical workstation. The whole system was placed under standard AM 1.5 G solar illumination simulated with a Xe lamp (Perfect Light PLS-SXE300c, 300 W). A mixed solution of 0.25 M Na_2S and 0.35 M Na_2SO_3 was used as the electrolyte and sacrificial agent.

Calculation methods

DFT calculations were performed with the plane-wave basis code Vienna *Ab initio* Simulation Package (VASP).[39] A plane-wave cutoff of 500 eV was used, and an 8 × 8 × 6 Monkhorst–Pack *k*-point grid was adopted for calculations on ZnO and ZnS and SNSs. A slab-model of SNSs with a supercell size of $a = b = 3.43208$ Å, $c = 27.63690$ Å, $\alpha = \beta = 90°$, and $\gamma = 60°$ was used in the calculations. By using a conjugate gradient method, all atomic positions and lattice constants were optimized, where the total energy and atomic forces were minimized. The total energy difference between two electronic steps was less than 10^{-5} eV, and the convergence criterion of the Hellmann–Feynman force on each atom was 0.01 eV $Å^{-1}$ during the ionic relaxation. For electronic structure calculations, the Heyd–Scuseria–Ernzerhof (HSE) hybrid functional was used to estimate the band gap.[40,41] The Hartree–Fock mixing parameter was set to 0.325 in HSE calculations.

Results and discussion

The as-prepared ZnS/ZnO/ZnS SNSs were characterized using a set of techniques, as shown in Fig. 1. The atomic force microscopy (AFM) image in Fig. 1a presents several SNSs with a size of several microns and a thickness of ~4.4 nm. Comparison with the initial ZnS/Zn/ZnS nanosheets prepared *via* thermal evaporation (Fig. S1,† the synthetic mechanism will be discussed in a future study) shows that annealing treatment did not change the initial morphology and only resulted in a slight gain in thickness due to oxidation (Fig. S2†). The initial ZnS/Zn/ZnS nanosheets are mainly composed of metallic Zn according to the XRD profile (Fig. S3†) and contain a small amount of the S element according to the XPS results (Fig. S4†). During the oxidation process, the inner Zn was oxidized to ZnO at a temperature of 553 K, while the inert ZnS outer layer remained intact, leading to a ZnS/ZnO/ZnS sandwich structure. The SEM (Fig. S5†) and TEM (Fig. S6†) images reveal its sheet-like morphology with a size of around 4.3 μm. The side-view high-resolution TEM (HRTEM) image in Fig. 1b shows different lattice spacings at the surface and interior of the nanosheet, 0.31 and 0.26 nm, which correspond to the (0002) plane of ZnS and ZnO, respectively. It is worth noting that the lattices related to ZnS are limited to one or two atomic layers, suggesting the existence of an atomically thin surface ZnS layer. The elemental line scanning analysis of the K edge of the sulfur element shows that the S element is distributed merely at the surface of SNSs (Fig. S7†). Meanwhile, the energy filtered TEM

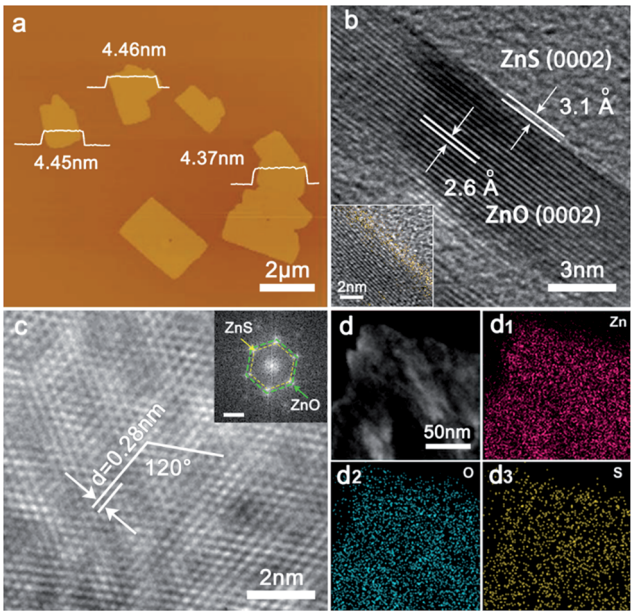

Fig. 1 Characterization of ZnS/ZnO/ZnS SNSs. (a) AFM images of several nanosheets. (b) Side-view HRTEM of a sandwich nanosheet. The inset shows an overlapped side-view TEM image with the energy-filtered image of the S element. (c) Plane-view HRTEM image of a SNS and its corresponding fast Fourier transform image. (d) HAADF-STEM image of a nanosheet and (d1–d3) EDX elemental mapping images of Zn, O, and S of the same nanosheet, respectively.

(EFTEM) image (the inset of Fig. 1b) clearly illustrates that S atoms are confined in a thin surface layer of about 1 nm, thus confirming the existence of a surface ZnS layer. The HRTEM image in Fig. 1c only shows the lattice fringes of ZnO. However, the fast Fourier transform (FFT) pattern in the inset of Fig. 1c contains two sets of spots related to diffraction patterns along the [0001] axis, suggesting the co-existence of ZnS and ZnO phases with their (0002) planes connected to each other. The SAED pattern taken from a larger area also supports this finding (see the inset in Fig. S6b†). At the same time, the XRD pattern exhibited distinct peaks matching well with those of the ZnO phase, while those of the ZnS phase were very weak (Fig. S8†), which agrees well with those of atomically-thin ZnS. The high-angle annular dark field scanning TEM (HAADF-STEM) image (Fig. 1d) shows that Zn and O are homogeneously distributed throughout the nanosheet, while the S signal is rather weak, implying a thin ZnS layer over its ZnO substrate. The XPS survey scan spectrum of the SNSs only exhibited the peaks of Zn, O, and S, apart from a C peak caused by surface contaminations (Fig. S9a†), while the narrow-scan spectra indicated the existence of Zn^{2+}, O^{2-} and S^{2-} ions (Figs. S9b–d†), the latter S2p peak being very weak (Fig. S9d†). The Zn peaks located at 1021.36 eV and 1044.45 eV corresponded to Zn 2p 3/2 and 2p 1/2, respectively. Interestingly, the lattice oxygen position shifts slightly from 530.03 eV of ZnO NSs to 530.08 eV of SNSs, which arises from the influence of the surface S element on the adjacent O atoms. Besides, the extremely low S 2p peak can be attributed to the ultrathin ZnS overlayer and then the ultralow S content in the SNS sample.

The high-resolution AFM images revealed significant fluctuations in the thickness of the as-prepared SNSs (Fig. S10†), suggesting that the surface ZnS layer might be somewhat discrete. To lend support to this hypothesis, we etched a nanosheet by means of acetic acid which is known to dissolve only ZnO. The inner ZnO was found to be etched homogenously (Fig. S11†), leaving a pure ZnS layer, as determined by XPS (Fig. S12†). This phenomenon implies that the ZnS overlayer is not continuous; otherwise, the etching should proceed from the edge to the centre of the nanosheet. As shown in the TEM image (Fig. S13†), the residual ZnS layer shows a porous morphology with very low contrast. The AFM image shown in Fig. S14† reveals that the thickness of the ZnS is only 0.66–0.67 nm, corresponding to one or two atomic layers. More evidence comes from the cross-sectional HRTEM image of the SNSs in Fig. S15,† where the outermost surface layer seems not even, some of its parts having the lattice spacing of ZnS (0.31 nm), while others showing that of ZnO (0.27 nm).

In brief, the as-prepared ZnS/ZnO/ZnS SNSs have a ZnO substrate and porous atomically thin layers of ZnS. Using similar recipes, we also prepared pure ZnO and ZnS NSs with the same morphology (Fig. S16†) and thickness (Fig. S17†), as well as a similar specific surface area (Fig. S18†), so that the performance of these three kinds of NSs could be compared.

Fig. 2 compares hydrogen evolution of the SNSs and their ZnO and ZnS counterparts with the same sizes and morphology. The dose of photocatalysts was set as 10 mg in 40 mL solution according to the relationship between usage and photocatalytic performance (Fig. S19†). The SNS material as seen in Fig. 2a exhibits the highest mass-specific activity (2.08 mmol h^{-1} g^{-1}) under full-spectrum light, which is significantly larger than that of ZnO (0.11 mmol h^{-1} g^{-1}) or ZnS (0.18 mmol h^{-1} g^{-1}). In comparison with the ZnO NSs, the ZnS NSs exhibit a higher hydrogen production efficiency, because their higher conduction band ensures higher energy electrons for water reduction.[32] The photocatalytic properties demonstrated by the novel material are among the best ever reported for ZnO and ZnS photocatalysts without a co-catalyst. Under visible light (λ > 400 nm, Fig. 2b), the difference in performance is also very prominent, as the hydrogen evolution rate of the SNSs (79.8 μmol h^{-1} g^{-1}) is almost one order of magnitude higher than those of the ZnO (8.15 μmol h^{-1} g^{-1}) and ZnS (11.1 μmol h^{-1} g^{-1}) NSs. Under ultraviolet light (320 nm < λ < 400 nm, Fig. S20†), the SNSs also exhibit excellent photocatalytic activity with a hydrogen evolution rate of 22.7 mmol h^{-1} g^{-1}. In the absence of sacrificial agents (Na_2S and Na_2SO_3), both ZnS and ZnO do not show obvious photocatalytic activity any more, while the SNSs still produce hydrogen gas under full-spectrum light irradiation (Fig. S21†), which should be attributed to their appropriate band structure (see Fig. 3a). Moreover, the SNS material shows excellent reusability; after separation and redispersion, the total photocatalytic H_2 production merely decreases by 9.6%, which may originate from the aggregation of the nanosheets (Fig. S22†).

In addition, the photocatalytic stability of all three materials was tested. As shown in Fig. 2c, the hydrogen evolution rate of the SNSs was mainly unchanged after 20 h, without a noticeable decrease in each cycling test, while the performance of the ZnO and ZnS was found to deteriorate over time. The quantum yield (QE) of the photocatalysts can be calculated as the number of evolved H_2 molecules divided by the actual absorption intensity (see details in the ESI†). The QE of the SNSs was found to reach as much as 34.7%, whereas that of the ZnO NSs (Fig. S23†) was only 4.8% at 420 nm. Compared with previously reported ZnO- or ZnS-based materials with different morphologies and additives, our SNSs have the highest quantum yield.[33,35,42,43]

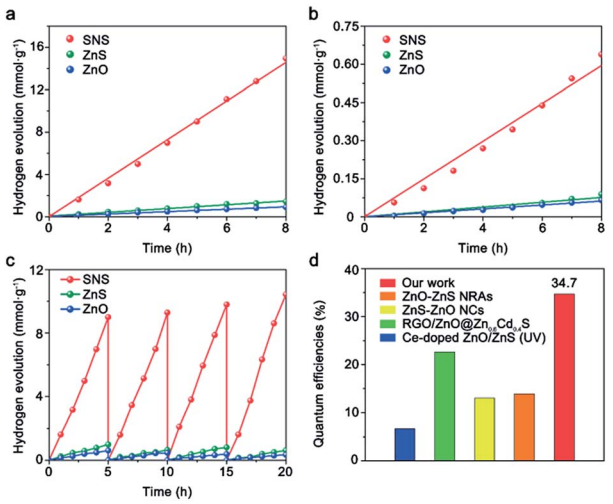

Fig. 2 Photocatalytic H_2 production of SNSs, ZnS NSs, and ZnO NSs. (a) Hydrogen evolution under simulated air mass 1.5 solar illumination. (b) Under visible light with λ > 400 nm. (c) Cyclic tests under sunlight. (d) Comparison of photocatalytic quantum efficiencies of SNSs with those of relevant materials reported in the literature.[32,34,38,42]

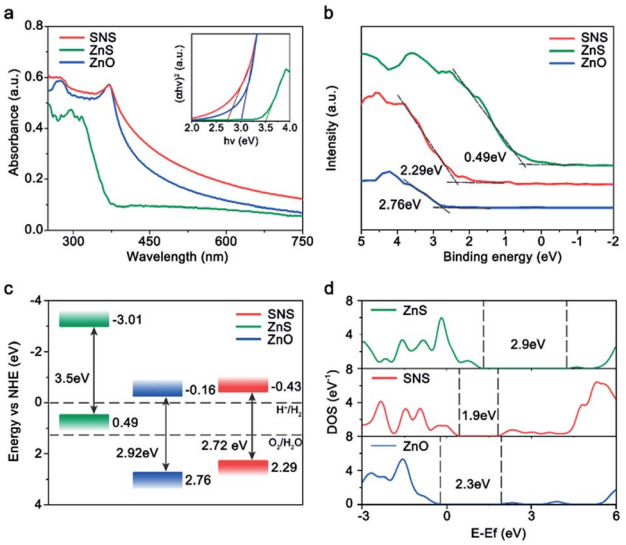

Fig. 3 Band structures of SNSs, ZnS NSs, and ZnO NSs. (a) Diffuse reflectance ultraviolet-visible spectra. The inset shows the plots of transformed Kubelka–Munk function *vs.* light energy. (b) Valence-band XPS spectra. (c) Energy level diagram. (d) Density of states (DOSs) calculated using the HSE06 functional, with the Fermi level set at 0 eV. Vertical dashed lines indicate the positions of the highest occupied and lowest unoccupied states.

Fig. 3a compares the UV-Vis absorption spectra of the SNSs, ZnO NSs and ZnS NSs deposited onto FTO and then measured using a solid integrating sphere. The inset in Fig. 3a presents transformed Kubelka–Munk functions *versus* light energy, which indicate band-gap energies of 2.72, 2.92 and 3.5 eV for the SNSs, and ZnO and ZnS NSs, respectively. The measured band gaps of the ZnO and ZnS NSs are seen to be much lower than those of their bulk counterparts (3.3 eV for ZnO and 3.7 eV for ZnS), which may result from the large exposed surface area and related surface states.[44] As for the narrow band gap of the SNSs, recently Torabi and Staroverov proposed that the band gap of a thin ZnO film can be reduced by means of a surface ZnS layer as a result of the covariate effect of these two materials.[38] On the other hand, from the valence band XPS spectra in Fig. 3b, the valence band positions of the SNSs, and ZnO and ZnS NSs could be determined to be 2.42, 2.76, and 0.49 eV, respectively. Accordingly, the band structure diagrams drawn using these values are given in Fig. 3c. The conduction band level of the SNSs is seen to be slightly higher than that of the ZnO NSs, which is believed to contribute positively to reduction of H_2O to H_2.

To understand the appearance of the narrow band gap in the novel material, we established the structural models of layered SNSs, ZnO, and ZnS for density functional theory (DFT) calculations (Fig. S24 and S25†). Having started with ten (0001) monolayers of ZnO (*i.e.*, monolayers normal to the [0001] direction), we then replaced two of the outermost layers with the (0001) monolayers of ZnS. The results of our computations are presented in Fig. 3d and S26.† The results depict that the band gap significantly decreases from 2.3 eV for pure ZnO to 1.9 eV for the SNSs after ZnS layers are incorporated into the pure ZnO phase. Although the band gap calculated for the SNSs was smaller than the experimentally observed value, which is easily explained by the use of a simplified model, the DFT calculations clearly attest that an atomically thin surface ZnS layer can change the electronic structure of the ZnO substrate and reduce its band gap.

Further, using the pure ZnO NSs as the reference, we investigated the charge separation dynamics of the SNSs according to the electron lifetime (τ_n) of photoanodes, which can be calculated from the Bode phase plots (Fig. 4a) using eqn (3):

$$\tau_n = 1/(2\pi f_{max}) \quad (3)$$

where, f_{max} is the maximum frequency value and τ_n is the electron lifetime. As seen in Fig. 4a, the f_{max} of the SNSs is 20 Hz, which is smaller than that of pure ZnO NSs (63 Hz). Accordingly, the calculated electron lifetimes of the SNSs and ZnO NSs are 7.9 and 2.5 ms, respectively. The longer electron lifetime found for the SNS sample suggests slower electron–hole recombination in this material, indicating rather advantageous charge separation processes.[45]

Photoluminescence (PL) spectra are known as a potential source of information on electron–hole recombination; which is why such spectra for the ZnO and SNS materials are presented in Fig. 4b. The pure ZnO NSs exhibit strong PL peaks at 387 nm and 620 nm, which arise from intrinsic and defect-related light emission, respectively.[46,47] In contrast, both defect-related and intrinsic PL peaks are quenched in the SNSs, implying that the surface ZnS layer not only eliminates defects *via* passivation, but also suppresses the electron–hole recombination.

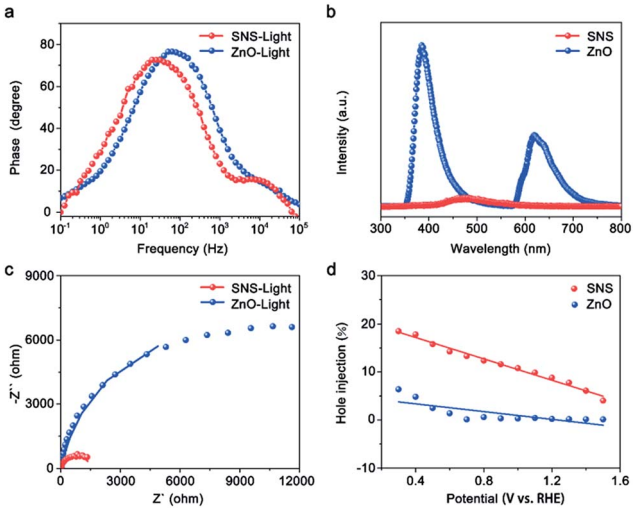

Fig. 4 Charge separation in SNSs and ZnO NSs. (a) Bode phase plots. (b) Photoluminescence spectra. (c) Nyquist plots of their EIS spectra measured at 0 V *vs.* Ag/AgCl under 1 sun AM 1.5G illumination. (d) Hole injection rates derived from photocurrent densities without and with the hole scavengers.

The interface transfer resistance of the ZnO and SNSs was tested by means of electrochemical impedance spectroscopy (EIS). For this, both materials were assembled into photoanodes for photoelectrochemical measurements at 0 V *vs.* Ag/AgCl under AM 1.5 illumination, their Nyquist plots being presented in Fig. 4c. The corresponding equivalent circuit model is shown in Fig. S27,† where R_s represents the resistance of the electrolyte, CPE is the capacitance phase element and R_{ct} is the charge transfer resistance between the photoanode and the electrolyte. By fitting the Nyquist plots with the given model, the values of R_{ct} for the ZnO NSs and SNSs were determined to be 15 362 and 1479 Ω, respectively. This indicates that the hole transfer through the solid/liquid interface in the novel sandwich material is much more favorable. Thus, we conclude that the surface ZnS layer catalyzes the reaction between the hole and the sacrificial agent so that holes can be quickly consumed.

Finally, we investigated how the ZnS layer affects hole injection into the electrolyte by calculating the rate of hole injection using eqn (4):[48]

$$P_{\text{hole injection}} = J^{H_2O}_{\text{photocurrent}} \Big/ J^{Na_2S/Na_2SO_3}_{\text{photocurrent}} \quad (4)$$

where, $J^{H_2O}_{\text{photocurrent}}$ and $J^{Na_2S/Na_2SO_3}_{\text{photocurrent}}$ are the photocurrent densities without and with the hole scavengers, which are given in Fig. S28 and S29,† respectively. In comparison with the ZnO NSs, the photocurrent of the SNSs changes more significantly in the dark and under light irradiation, indicating higher charge separation efficiency. As seen in Fig. 4d, the values obtained for the ZnO NSs remain at a lower level, from 0.1% at 1.5 V to 6.4% at a voltage of 0.3 V. In contrast, the SNSs demonstrate a rather

high hole injection rate, from 4.0% at 1.5 V to 18.5% at 0.3 V, suggesting that the topmost ZnS layer can lower the resistance at the electrode/electrolyte interface and accelerate hole transfer. The found high hole injection rate agrees well with the results of EIS.

We also recovered the tested ZnO NSs and SNSs (denoted as ZnO-R and SNS-R) and made comprehensive characterization. According to the XRD results (Fig. S30†), the ZnO NSs completely transformed into ZnS after 4 cycles of testing, due to the reaction with the sulfur-containing sacrificial reagents (Na_2S and Na_2SO_3);[50,51] at the same time, the morphology changed from nanosheet into nanoparticle (Fig. S31a and S32a–b†). In contrast, under the protection of the ZnS layer, most of ZnO in the SNSs was preserved after 4 rounds of testing (Fig. S30†), keeping the nanosheet morphology intact (Fig. S31b and S32c–d†). Nevertheless, XRD analysis indicates weak vulcanization of the SNSs during water splitting since the amount of ZnS slightly increases in SNS-R (Fig. S30†). This observation correlates with the red shift of the absorption edge of the SNSs in the DRS profile (Fig. S33†).[49] Thus, the concentration of the sacrificial agents should be kept at a rather low level; otherwise, the photocatalytic activity of the SNSs may deteriorate remarkably due to the serious vulcanization of ZnO (Fig. S34†).

Based on the above mentioned results, the improved performance of the novel SNSs during water splitting can be explained as follows. As shown in Fig. 5, the SNSs are comprised of ultra-thin ZnO cores and atomically thin porous ZnS layers. Importantly, the outer ZnS layer is not continuous, making the internal ZnO partially exposed and giving rise to a hybrid surface with ZnO pits embedded into the ZnS skin. When irradiated with sunlight, such SNSs with a narrower band gap can absorb incident light in a broader spectral range and generate more electron–hole pairs than their ZnO counterpart. Meanwhile, a built-in electric field forms between the exposed Zn^{2+} plane of the ZnO pits and the S^{2-} plane of the ZnS skin due to their different chemical potentials. This electric field can drive the migration of electrons and holes toward ZnO and ZnS areas, respectively, leading to rapid charge separation (see the enlarged portion in Fig. 5), which is proven by the longer electron lifetime and quenched PL in the SNSs. Subsequently, the holes are immediately consumed by the sacrificial agent (Na_2S/Na_2SO_3 in our case) under the catalysis of the surface ZnS layer, while the electrons remain safely on the ZnO surface where they gradually reduce H^+ ions to produce H_2 gas.

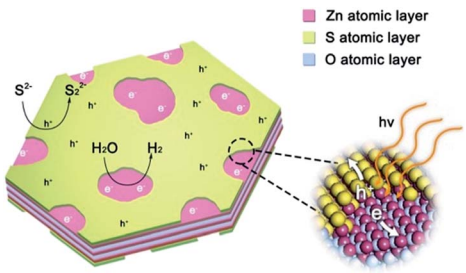

Fig. 5 Schematic structure of the ZnS/ZnO/ZnS SNS and hydrogen production on its surface. Yellow color indicates S atoms, pink color stands for Zn, and light-blue color depicts oxygen layers.

Conclusion

Sandwich nanosheets with an ultra-thin ZnO core and surface layers of ZnS were engineered in this study. When compared with its ZnO counterpart, the newly designed sandwich structure shows several unique features. First, the modification of the surface with a ZnS layer leads to a noticeable reduction in the band gap, which manifests in the extension of the absorption spectrum and more efficient absorption and use of natural light. Simultaneously, the conduction band position of the sandwich nanostructure does not decrease, even slightly increasing with respect to that of ZnO, thereby maintaining the reducing capability of photo-excited electrons. Second, the ultra-low thickness and hybrid ZnO/ZnS surface of the novel material shorten the diffusion length of holes and electrons, thus speeding up the charge separation. Third, the surface ZnS layers catalyze the reaction of holes with sacrificial agents, thus reducing hole accumulation, suppressing light corrosion and providing high stability to the novel sandwich nanostructure. Fourth, the surface ZnS layers prevent ZnO from being vulcanized, thus achieving high stability. As a result, the newly prepared ZnS/ZnO/ZnS nanosheets achieve superior activity for hydrogen production, which is one order of magnitude higher than that of their pure ZnO counterpart. The excellent performance demonstrated by this novel material suggests that it is a very promising candidate for efficient and stable catalysis for water splitting.

Conflicts of interest

There are no conflicts to declare.

Acknowledgements

This work was supported by the National Basic Research Program of China (2014CB931703) and the National Natural Science Foundation of China (No. 51671141, 51571149, and 51471115).

Notes and references

1 A. Fujishima and K. Honda, *Nature*, 1972, **238**, 37–38.
2 X. G. Meng, L. Liu, S. X. Ouyang, H. Xu, D. F. Wang, N. Q. Zhao and J. H. Ye, *Adv. Mater.*, 2016, **28**, 6781–6803.
3 S. Y. Tee, K. Y. Win, W. S. Teo, L. D. Koh, S. H. Liu, C. P. Teng and M. Y. Han, *Adv. Sci.*, 2017, **4**, 1600337.
4 J. Qi, W. Zhang and R. Cao, *Adv. Energy Mater.*, 2017, 1701620.
5 Y. Q. Qu and X. F. Duan, *Chem. Soc. Rev.*, 2013, **42**, 2568.
6 Q. P. Lu, Y. F. Yu, Q. L. Ma, B. Chen and H. Zhang, *Adv. Mater.*, 2016, **28**, 1917–1933.
7 H. L. Zhou, Y. Q. Qu, T. Zeida and X. F. Duan, *Energy Environ. Sci.*, 2012, **5**, 6732–6743.
8 R. Marschall, *Adv. Funct. Mater.*, 2014, **24**, 2421–2440.

9 J. T. Li and N. Q. Wu, *Catal. Sci. Technol.*, 2015, **5**, 1360–1384.
10 S. Y. Chen and L. W. Wang, *Chem. Mater.*, 2012, **24**, 3659–3808.
11 K. Li, M. Han, R. Chen, S. L. Li, S. L. Xie, C. Y. Mao, X. H. Bu, X. L. Cao, L. Z. Dong, P. Y. Feng and Y. Q. Lan, *Adv. Mater.*, 2016, **28**, 8906–8911.
12 J. A. del Alamo, *Nature*, 2011, **479**, 317–323.
13 R. E. Nahory, M. A. Pollack, W. D. Johnston Jr and R. L. Barns, *Appl. Phys. Lett.*, 1978, **33**, 659–661.
14 J. Y. Feng, D. P. Cao, Z. Q. Wang, W. J. Luo, J. J. Wang, Z. S. Li and Z. G. Zou, *Chem.–Eur. J.*, 2014, **20**, 16384–16390.
15 J. W. Fu, J. G. Yu, C. J. Jiang and B. Cheng, *Adv. Energy Mater.*, 2017, 1701503.
16 M. Z. Ge, Q. S. Li, C. Y. Cao, J. Y. Huang, S. H. Li, S. N. Zhang, Z. Chen, K. Q. Zhang, S. S. Al-Deyab and Y. K. Lai, *Adv. Sci.*, 2017, **4**, 1600152.
17 Y. Q. Yang, G. Liu, J. T. S. Irvine and H. M. Cheng, *Adv. Mater.*, 2016, **28**, 5850.
18 M. H. Hsu, C. J. Chang and H. T. Weng, *ACS Sustainable Chem. Eng.*, 2016, **4**, 1381–1391.
19 Y. H. Lu, W. H. Lin, C. Y. Yang, Y. H. Chiu, Y. C. Pu, M. H. Lee, Y. C. Tsenga and Y. J. Hsu, *Nanoscale*, 2014, **6**, 8796–8803.
20 Z. H. Zhao, J. Tian, Y. H. Sang, A. Cabot and H. Liu, *Adv. Mater.*, 2015, **27**, 2557–2582.
21 B. A. F. Taghipour, *Chem. Eng. Technol.*, 2016, **39**, 142–148.
22 K. Maeda, T. Takata, M. Hara, N. Saito, Y. Inoue, H. Kobayashi and K. Domen, *J. Am. Chem. Soc.*, 2005, **127**, 8286–8287.
23 H. M. Chen, C. K. Chen, R. S. Liu, C. C. Wu, W. S. Chang, K. H. Chen, T. S. Chan, J. F. Lee and D. P. Tsai, *Adv. Energy Mater.*, 2011, **1**, 742–747.
24 T. F. Yeh, C. Y. Teng, S. J. Chen and H. Teng, *Adv. Energy Mater.*, 2014, **26**, 3297–3303.
25 J. Wang, Y. Xia, Y. Dong, R. S. Chen, L. Xiang and S. Komarneni, *Appl. Catal., B*, 2016, **192**, 8–16.
26 I. Lee, J. B. Joo, Y. D. Yin and F. Zaera, *Angew. Chem.*, 2011, **123**, 10390–10393.
27 S. S. Zhu and D. W. Wang, *Adv. Energy Mater.*, 2017, 1700841.
28 Y. J. Zou, J. W. Shi, D. D. Ma, Z. Y. Fan, C. M. Niu and L. Z. Wang, *ChemCatChem*, 2017, **9**, 3752–3761.
29 X. X. Zou, P. P. Wang, C. G. Li, J. Zhao, D. J. Wang, T. Asefa and G. D. Li, *J. Mater. Chem. A*, 2014, **2**, 4682–4689.
30 Q. Simon, D. Barreca, A. Gasparotto, C. Maccato, T. Montini, V. Gombac, P. Fornasiero, O. I. Lebedev, S. Turner and G. V. Tendeloo, *J. Mater. Chem.*, 2012, **22**, 11739–11747.
31 S. Cho, J. W. Jang, J. W. Kim, J. S. Lee, W. Y. Choi and K. H. Lee, *Langmuir*, 2011, **27**, 10243–10250.
32 D. Bao, P. Gao, Y. J. Chen, X. Y. Zhu, H. Zhou, S. C. Sun, Y. B. Wang, Y. Wang and P. P. Yang, *Chem.–Eur. J.*, 2015, **21**, 12728–12734.
33 W. W. He, H. M. Jia, J. H. Cai, X. N. Han, Z. Zheng, W. G. Wamer and J. J. Yin, *J. Phys. Chem. C*, 2016, **120**, 3187–3195.
34 Z. Wang, S. W. Cao, S. C. J. Loo and C. Xue, *CrystEngComm*, 2013, **15**, 5688–5693.
35 J. X. Low, J. G. Yu, M. Jaroniec, S. Wageh and A. A. Al-Ghamdi, *Adv. Mater.*, 2017, **29**, 1601694.
36 M. Zhou, X. W. (David) Lou and Y. Xie, *Nano Today*, 2013, **8**, 598–618.
37 X. W. Wang, L. C. Yin, G. Liu, L. Z. Wang, R. Saito, G. Q. (Max) Lu and H. M. Cheng, *Energy Environ. Sci.*, 2011, **4**, 3976–3979.
38 A. Torabi and V. N. Staroverov, *J. Phys. Chem. Lett.*, 2015, **6**, 2075–2080.
39 G. Kresse and J. Hafner, *Phys. Rev. B: Condens. Matter Mater. Phys.*, 1994, **49**, 14251–14269.
40 H. Jochen, G. E. Scuseria and M. Ernzerhof, *J. Chem. Phys.*, 2003, **118**, 8207–8215.
41 H. Jochen, G. E. Scuseria and M. Ernzerhof, *J. Chem. Phys.*, 2006, **124**, 219906.
42 W. Kang, J. M. Xu and X. T. Wang, *Appl. Surf. Sci.*, 2016, **360**, 270–275.
43 C. J. Chang, K. L. Huang, J. K. Chen, K. W. Chu and M. H. Hsu, *J. Taiwan Inst. Chem. Eng.*, 2015, **55**, 82–89.
44 Y. F. Sun, Z. H. Sun, S. Gao, H. Cheng, Q. H. Liu, J. Y. Piao, T. Yao, C. Z. Wu, S. L. Hu, S. Q. Wei and Y. Xie, *Nat. Commun.*, 2012, **3**, 1057.
45 Y. R. Lu, P. F. Yin, J. Mao, M. J. Ning, Y. Z. Zhou, C. K. Dong, T. Ling and X. W. Du, *J. Mater. Chem. A*, 2015, **3**, 18521–18527.
46 A. Umar and Y. B. Hahn, *Appl. Phys. Lett.*, 2006, **88**, 173120.
47 C. C. Li, T. Wang, Z. B. Luo, D. Zhang and J. L. Gong, *Chem. Commun.*, 2015, **51**, 7290–7293.
48 J. P. Song, P. F. Yin, J. Mao, S. Z. Qiao and X. W. Du, *Nanoscale*, 2017, **9**, 6296–6301.
49 H. Zhao, Y. M. Dong, P. P. Jiang, G. L. Wang, H. Y. Miao, R. X. Wu, L. G. Kong, J. J. Zhang and C. Zhang, *ACS Sustainable Chem. Eng.*, 2015, **3**(5), 969–977.
50 S. Kumar, N. L. Reddy, H. S. Kushwaha, A. Kumar, M. V. Shankar, K. Bhattacharyya, A. Halder and V. Krishnan, *ChemSusChem*, 2017, **10**, 3588–3603.
51 P. Gomathisankar, K. Hachisuka, H. Katsumata, T. Suzuki, K. Funasaka and S. Kaneco, *ACS Sustainable Chem. Eng.*, 2013, **1**, 982–988.
52 S. S. Kai, B. J. Xi, X. L. Liu, L. Ju, P. Wang, Z. Y. Feng, X. J. Ma and S. L. Xiong, *J. Mater. Chem. A*, 2018, **6**, 2895–2899.
53 S. S. Kai, B. J. Xi, Y. F. Wang and S. L. Xiong, *Chem.–Eur. J.*, 2017, **23**, 16653–16659.